Hydrodynamic Interaction Between Two Flexible Finite Length Coaxial Cylinders: New Theoretical Formulation and Numerical Validation

Romain Lagrange, Maria Adela Puscas

▶ **To cite this version:**

Romain Lagrange, Maria Adela Puscas. Hydrodynamic Interaction Between Two Flexible Finite Length Coaxial Cylinders: New Theoretical Formulation and Numerical Validation. Journal of Applied Mechanics, 2022, 89 (8), 10.1115/1.4054793 . hal-04019716

HAL Id: hal-04019716
https://hal.science/hal-04019716

Submitted on 3 Aug 2023

HAL is a multi-disciplinary open access archive for the deposit and dissemination of scientific research documents, whether they are published or not. The documents may come from teaching and research institutions in France or abroad, or from public or private research centers.

L'archive ouverte pluridisciplinaire **HAL**, est destinée au dépôt et à la diffusion de documents scientifiques de niveau recherche, publiés ou non, émanant des établissements d'enseignement et de recherche français ou étrangers, des laboratoires publics ou privés.

Hydrodynamic interaction between two flexible finite length coaxial cylinders: new theoretical formulation and numerical validation.

Romain Lagrange[a], Maria Adela Puscas[b]

[a] *Université Paris-Saclay, CEA, Service d'Etudes Mécaniques et Thermiques, F-91191, Gif-sur-Yvette, France*
[b] *Université Paris-Saclay, CEA, Service de Thermo-hydraulique et de Mécanique des Fluides, F-91191, Gif-sur-Yvette, France*

Abstract

This paper addresses the interaction of two coaxial cylinders separated by a thin fluid layer. The cylinders are flexible, have a finite length, and are subject to a vibration mode of an Euler-Bernoulli beam. Assuming a narrow channel, an inviscid and linear theoretical approach is carried out, leading to a new simple and tractable analytical expression of the fluid forces. We show that the dimensionless form of the fluid forces matrix reduces to a single coefficient whose properties (sign and variations) strongly depend on the boundary conditions, the wave-number of the vibration modes, and the aspect ratio of the cylinders. All these properties are made explicit in our formulation, which applies to all classical types of boundary conditions. A numerical approach based on an Arbitrary Lagrange-Eulerian method is also presented and successfully compared to the theoretical predictions.

Keywords: Fluid-Structure Interaction; Fluid forces, Coaxial cylinders; Narrow annulus

1. Introduction

This study finds its motivation in the understanding of the vibrations of guide tubes used in the Jules Horowitz Reactor. This test reactor was built primarily for research into materials and fuels for the nuclear power industry and nuclear medicine, see [1] for more details. The guide tubes are cylindrical structures made of aluminum, with a length of 2.1 m and an outer diameter of $2R_1 = 40$ mm. These tubes are used to guide the drive mechanism and the experimental equipment under test and are inserted into the cylindrical free space between the fuel assemblies. The diameter of the free space is $2R_2 = 44$ mm, so that the central part of the guide tubes is strongly constricted, with a 2 mm clearance, see Fig. 1. Like the fuel elements, the guide tubes are exposed to an axial flow from the primary circuit, with a characteristic velocity of 15 m/s in the middle part. Here, we consider the fluid-structure interaction problem corresponding to the particular configuration in which there is no axial flow but in which both the cylindrical fuel assembly and the guide tube vibrate. As the fuel element is of length $L = 700$ mm, the aspect ratio $L/R_1 = 35$ is not large enough to apply the two-dimensional potential flow theory and the slender-body approximation presented in [2, 3, 4, 5, 6, 7, 8] to estimate the fluid force matrix. Thus, it is necessary to develop a three-dimensional theory that accounts for the finite size of the tube and the confinement of the configuration, which affects the intensity of the fluid forces, as shown in [2, 9, 10, 11, 12]. The three-dimensional calculation of the fluid force acting on a flexible cylinder vibrating in a narrow coaxial cylindrical duct can be solved following the approach of [13]. However, this approach is not flexible enough to be used in an engineering environment as it yields a non-closed form solution for the fluid forces. Also, it does not cover the possibility of a fully flexible duct in which both the inner and outer cylinders are imposed different modes of vibration. Here, we carry out a three-dimensional inviscid theory and use the simplifying assumption of a narrow annulus, see [14, 15], to provide a very tractable method that yields a new analytical formulation of the fluid force matrix. This formulation does not rely on the slender-body approximation so that it is applicable to cylinders of any size. Also, it considers the possibility of a fully flexible duct covering all types of classical boundary conditions.

Email addresses: romain.lagrange@cea.fr (Romain Lagrange), romain.g.lagrange@gmail.com (Romain Lagrange)

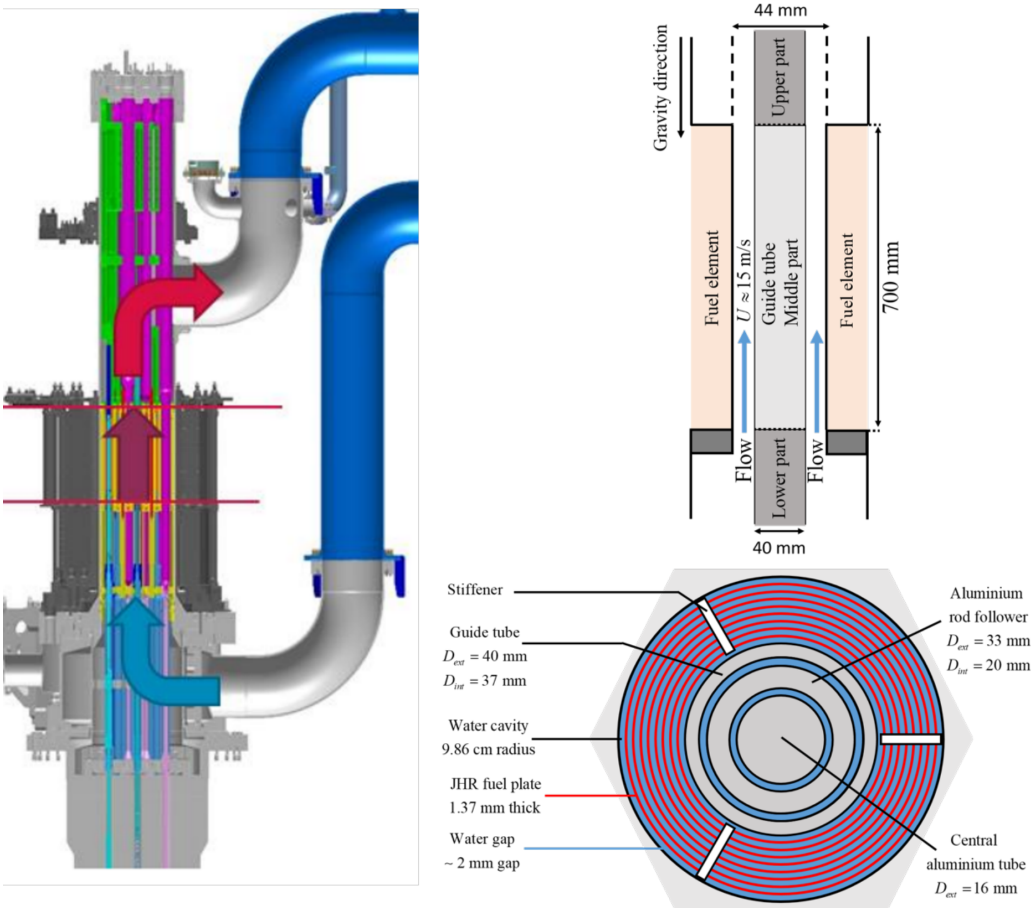

Figure 1: Left: sketch of the Jules Horowitz reactor (JHR), from [16]. Right: axial and radial cross section of the JHR assembly cell.

The paper is organized as follows. The statement of the problem and the governing equations are presented in § 2. In § 3 and § 4 we carry out a new theoretical formulation to estimate the fluid force matrix. A comparison between theoretical predictions and numerical results is detailed in § 5. Finally, some conclusions are drawn in § 6.

2. Definition of the problem and governing equations

We consider the three-dimensional problem of two coaxial cylinders, $\mathcal{C}_1$ (inner cylinder) and $\mathcal{C}_2$ (external cylinder), with axes along $\mathbf{e}_x$, separated by a thin layer of fluid. The cylinder $\mathcal{C}_i$ is flexible and points on its lateral boundary are imposed a simple harmonic displacement $\Re\left\{\mathrm{e}^{\mathrm{i}\Omega_i T}\mathbf{Q}_i\left(X\right)\right\}$ with Ω_i the angular frequency, T the dimensional time, X the longitudinal coordinate, $\Re$ the real part operator and i the imaginary complex unit. The displacement profile is of the form

$$\mathbf{Q}_i(X) = Q_i(X)\mathbf{e}_y + \Theta_i(X)\mathbf{e}_x, \tag{1}$$

with

$$Q_i\left(X\right) = Q_i\,\frac{W_i\left(X\right)}{N_i}, \quad \Theta_i(X) = -R_i\frac{dQ_i}{dX}(X), \tag{2}$$

the displacement of the neutral axis and the displacement due to the rotation of the cross-sections, respectively. The rotational displacement Θ_i is set so that the cross-sections remain orthogonal to the cross axis. In equation (2), Q_i is the amplitude of the displacement, $W_i(X)$ a bending mode of vibration of an Euler-Bernoulli beam and $N_i = \sup\left(|W_i\left(X\right)|, X \in [0, L]\right)$ its infinite norm. The cylinder $\mathcal{C}_i$ has a length L_i, radius R_i, boundary ∂C_i with outward unit normal vectors $\mathbf{n}_i$, see Fig. 2. We note $\overline{R} = (R_1 + R_2)/2$ the mean radius and $L = L_1$ the confined length.

The fluid is Newtonian, homogeneous, of volume mass density ρ and dynamic viscosity ν. The Navier-Stokes

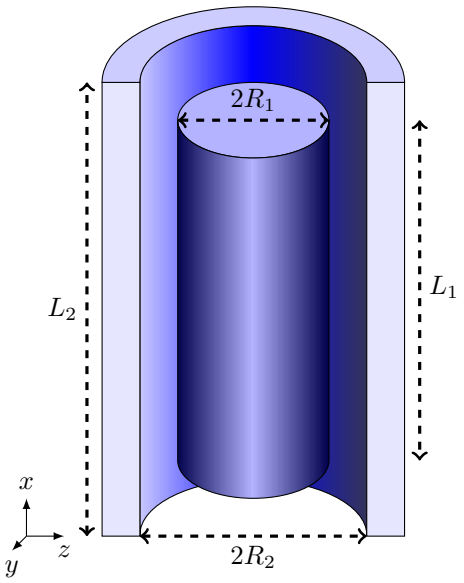

Figure 2: Two coaxial finite flexible cylinders in a narrow coaxial cylindrical channel.

equations for the incompressible fluid flow $(\mathbf{V}, P)$ write

$$\nabla \cdot \mathbf{V} = 0, \tag{3a}$$

$$\frac{\partial \mathbf{V}}{\partial T} + (\mathbf{V} \cdot \nabla)\,\mathbf{V} + \frac{1}{\rho}\nabla P - \nu \Delta \mathbf{V} = \mathbf{0}. \tag{3b}$$

Introducing the dimensionless fluid flow $(\mathbf{v}, p)$ as $\mathbf{V} = Q_i \Omega_i\ \mathbf{v}$ and $P = \rho\,(R_2 - R_1)\,Q_i \Omega_i^2\ p$, the dimensionless Navier-Stokes equations write

$$\nabla^* \cdot \mathbf{v} = 0, \tag{4a}$$

$$\frac{\partial \mathbf{v}}{\partial t} + \frac{Q_i}{R_2 - R_1}(\mathbf{v} \cdot \nabla^*)\,\mathbf{v} + \nabla^* p - \frac{\nu}{(R_2 - R_1)^2\,\Omega_i}\Delta^* \mathbf{v} = \mathbf{0}, \tag{4b}$$

with $t = \Omega_i T$ the dimensionless time and $\nabla^* = (R_2 - R_1)\,\nabla$ the dimensionless gradient operator. Assuming a small imposed amplitude of vibration compared to the size of the channel, i.e. $Q_i/(R_2 - R_1) \ll 1$, and an angular frequency Ω_i such that $(R_2 - R_1)^2\,\Omega_i/\nu \gg 1$, the nonlinear and viscous terms of the dimensionless Navier-Stokes equations are negligible. From the linearity of the problem, the fluid flow is $\Re\left\{\sum_{i=1}^{2} \mathrm{e}^{\mathrm{i}t}(\mathbf{v}_i, p_i)\right\}$ and the dimensionless Navier-Stokes equations along with the inviscid boundary conditions write

$$\nabla^* \cdot \mathbf{v}_i = 0, \tag{5a}$$

$$\mathrm{i}\mathbf{v}_i + \nabla^* p_i = \mathbf{0}, \tag{5b}$$

$$(\mathbf{v}_i - \mathrm{i}\mathbf{q}_i) \cdot \mathbf{n}_i = 0 \quad \text{on } \partial C_i, \tag{5c}$$

$$\mathbf{v}_i \cdot \mathbf{n}_j = 0 \quad \text{on } \partial C_j, \quad j \neq i, \tag{5d}$$

with $\mathbf{q}_i = w_i/N_i\ \mathbf{e}_y$ the dimensionless displacement and $w_i\,(x) = W_i\,(Lx)$ the vibration mode expressed in term of the dimensionless longitudinal coordinate $x = X/L$. The fluid-structure interaction is addressed through the boundary conditions (5c) and (5d) which express the continuity of the normal velocities at the boundary of the cylinders. This interaction yields a fluid force $\Re\left\{\sum_{j=1}^{2} \mathrm{e}^{\mathrm{i}\Omega_j T}\rho\pi R_i L R_j Q_j \Omega_j^2\ \mathbf{f}_{ij}\right\}$, with $\mathbf{f}_{ij}$ the dimensionless force acting on C_i, due to the motion of C_j. Assuming $\mathbf{n}_i \approx (-1)^{i+1}\,\mathbf{e}_r$ with $\mathbf{e}_r = \cos(\theta)\,\mathbf{e}_y + \sin(\theta)\,\mathbf{e}_z$ the unit polar direction and θ the polar angle, the dimensional inviscid fluid force $\mathbf{f}_{ij}$ is given by the integral of the total pressure field on ∂C_i. Introducing $\varepsilon = R_2/R_1$ as the radius ratio, the dimensionless fluid force writes

$$\begin{aligned} \mathbf{f}_{ij} &= (-1)^{i+1}\,\frac{R_2 - R_1}{R_j}\,\frac{1}{\pi}\int_0^1\int_0^{2\pi} -p_j\,(x,\theta)\mathbf{e}_r\,d\theta dx, \\ &\underset{\varepsilon \to 1}{\sim} (-1)^{i+1}\,(\varepsilon - 1)\,\frac{1}{\pi}\int_0^1\int_0^{2\pi} -p_j\,(x,\theta)\mathbf{e}_r\,d\theta dx. \end{aligned} \tag{6}$$

3. Theoretical pressure field

The divergence of equation (5b) shows that the pressure field is a harmonic function

$$\Delta^* p_i = \frac{\partial^2 p_i}{\partial r^2} + \frac{1}{r}\frac{\partial p_i}{\partial r} + \frac{1}{r^2}\frac{\partial^2 p_i}{\partial \theta^2} + \left(\frac{1}{\overline{r}\bar{l}}\right)^2 \frac{\partial^2 p_i}{\partial x^2} = 0, \tag{7}$$

with $(r, \theta, x) = (R/(R_2 - R_1), \theta, X/L)$ the dimensionless cylindrical coordinates and

$$\bar{l} = \frac{L}{\overline{R}} \underset{\varepsilon \to 1}{\sim} l = \frac{L}{R_1}, \quad \overline{r} = \frac{\overline{R}}{R_2 - R_1} \underset{\varepsilon \to 1}{\sim} \frac{1}{\varepsilon - 1}, \tag{8}$$

the aspect ratio and the dimensionless mean radius, respectively. Restricting the analysis to a narrow annulus, where $r \approx \overline{r}$, the Laplace equation (7) approximates to

$$\frac{1}{\overline{r}}\frac{\partial p_i}{\partial r} + \frac{1}{\overline{r}^2}\frac{\partial^2 p_i}{\partial \theta^2} + \left(\frac{1}{\overline{r}\bar{l}}\right)^2 \frac{\partial^2 p_i}{\partial x^2} = -\frac{\partial^2 p_i}{\partial r^2}. \tag{9}$$

Averaging equation (9) in the radial direction of the annulus yields

$$\frac{1}{\overline{r}}\left\langle \frac{\partial p_i}{\partial r} \right\rangle + \frac{1}{\overline{r}^2}\frac{\partial^2 \langle p_i \rangle}{\partial \theta^2} + \left(\frac{1}{\overline{r}\bar{l}}\right)^2 \frac{\partial^2 \langle p_i \rangle}{\partial x^2} = -\left[\frac{\partial p_i}{\partial r}\right]_{\partial C_i}^{\partial C_j}, \tag{10}$$

with $\langle p_i \rangle = \int_{R_1/(R_2-R_1)}^{R_2/(R_2-R_1)} p_i dr$. The first left hand side term writes $\left\langle \frac{\partial p_i}{\partial r} \right\rangle = \int_{r_1}^{r_2} \frac{\partial p_i}{\partial r} dr = p_i(r_2) - p_i(r_1)$, with $r_i = R_i/(R_2 - R_1)$ the dimensionless cylindrical coordinate of ∂C_i. Assuming that the pressure fluctuation $p_i(r_2) - p_i(r_1)$ is small compared with the average pressure $\langle p_i \rangle$ in the narrow annulus, this term is negligible compared to the second left hand side term of equation (10). The right hand side term is obtained from the projection of equation (5b) on $\mathbf{e}_r$. Using the boundary conditions equation (5c) and equation (5d) one obtains

$$\left.\frac{\partial p_i}{\partial r}\right|_{\partial C_i}^{\partial C_j} = \mathrm{i}\mathbf{v}_i \cdot \mathbf{e}_r \approx \mathrm{i}(-1)^{i+1} \mathbf{v}_i \cdot \mathbf{n}_i = -(-1)^{i+1} \frac{w_i}{N_i} \cos(\theta), \tag{11}$$

so that equation (10) approximates to

$$\frac{\partial^2 \langle p_i \rangle}{\partial x^2} + \bar{l}^2 \frac{\partial^2 \langle p_i \rangle}{\partial \theta^2} = \left(\overline{r}\bar{l}\right)^2 (-1)^{i+1} \frac{w_i}{N_i} \cos(\theta). \tag{12}$$

Seeking a solution as $\langle p_i \rangle = (-1)^{i+1} \overline{p_i}(x)/N_i \cos(\theta)$, equation (10) finally approximates

$$\frac{d^2 \overline{p_i}}{dx^2} - \bar{l}^2 \overline{p_i} = \left(\overline{r}\bar{l}\right)^2 w_i. \tag{13}$$

The forcing term w_i on the right hand side of equation (13) represents the bending mode of vibration which is imposed to the cylinder $\mathcal{C}_i$. Modeling this cylinder as an Euler-Bernoulli beam, w_i is a linear combination between trigonometric and hyperbolic functions,

$$w_i(x) = \chi_i^{(1)} \cosh(\lambda_i x) + \chi_i^{(2)} \cos(\lambda_i x) + \chi_i^{(3)} \sinh(\lambda_i x) + \chi_i^{(4)} \sin(\lambda_i x), \tag{14}$$

with $\chi_i^{(k)}$ some real coefficients which depend on the type of boundary conditions applied at the ends of the beam. To simplify the following developments, we write the displacement on a compact form, $w_i = \sum_{k=1}^{2} w_i^{(k)}$ with

$$w_i^{(k)}(x) = \chi_i^{(k)} \cos\left(\mathrm{i}^k \lambda_i x\right) + \chi_i^{(k+2)} (-\mathrm{i})^k \sin\left(\mathrm{i}^k \lambda_i x\right). \tag{15}$$

From the linearity of equation (13), the dimensionless pressure term $\overline{p_i}$ writes $\overline{p_i} = \sum_{k=1}^{2} \overline{p_i}^{(k)}$ with $\overline{p_i}^{(k)}$ satisfying

$$\frac{d^2 \overline{p_i}^{(k)}}{dx^2} - \bar{l}^2 \overline{p_i}^{(k)} = \left(\overline{r}\bar{l}\right)^2 w_i^{(k)}. \tag{16}$$

The solution of this linear equation is the sum of the solution of the homogeneous equation and a particular solution sought as a superposition of cosine and sine functions. This yields

$$\overline{p_i}^{(k)}(x) = -\left[\overline{r}^2 g_i^{(k)}\left(x, \bar{l}\right) + a_i^{(k)}\left(\bar{l}, \overline{r}\right) \mathrm{e}^{\bar{l}x} + b_i^{(k)}\left(\bar{l}, \overline{r}\right) \mathrm{e}^{-\bar{l}x}\right], \tag{17}$$

with

$$g_i^{(k)}\left(x,\bar{l}\right)=\frac{1}{1+(-1)^k\left(\lambda_i/\bar{l}\right)^2}w_i^{(k)}\left(x\right). \tag{18}$$

The functions $a_i^{(k)}$ and $b_i^{(k)}$ are determined with the dimensionless pressure conditions at both ends of the beam, namely $\overline{p_i}(0)$ and $\overline{p_i}(1)$

$$a_i^{(k)}\left(\bar{l},\bar{r}\right)+b_i^{(k)}\left(\bar{l},\bar{r}\right)=-\left[\overline{p_i}^{(k)}\left(0\right)+\bar{r}^2g_i^{(k)}\left(0,\bar{l}\right)\right], \tag{19a}$$

$$a_i^{(k)}\left(\bar{l},\bar{r}\right)\mathrm{e}^{\bar{l}}+b_i^{(k)}\left(\bar{l},\bar{r}\right)\mathrm{e}^{-\bar{l}}=-\left[\overline{p_i}^{(k)}\left(1\right)+\bar{r}^2g_i^{(k)}\left(1,\bar{l}\right)\right]. \tag{19b}$$

Solving the linear system (19) yields

$$a_i^{(k)}\left(\bar{l},\bar{r}\right)=b_i^{(k)}\left(-\bar{l},\bar{r}\right)=\frac{\left[\bar{r}^2g_i^{(k)}\left(0,\bar{l}\right)+\overline{p_i}^{(k)}\left(0\right)\right]\mathrm{e}^{-\bar{l}}-\left[\bar{r}^2g_i^{(k)}\left(1,\bar{l}\right)+\overline{p_i}^{(k)}\left(1\right)\right]}{2\sinh\left(\bar{l}\right)}, \tag{20}$$

so that the dimensionless pressure $\overline{p_i}^{(k)}$ generated by $w_i^{(k)}$ writes

$$\overline{p_i}^{(k)}\left(x\right)=-\left[\bar{r}^2g_i^{(k)}\left(x,\bar{l}\right)+\sum_{n=1}^{2}a_{in}^{(k)}\left(\bar{l},\bar{r}\right)\mathrm{e}^{(-1)^n\bar{l}x}\right], \tag{21}$$

with $a_{in}^{(k)}\left(\bar{l},\bar{r}\right)=a_i^{(k)}\left((-1)^n\bar{l},\bar{r}\right)$, i.e.

$$a_{in}^{(k)}\left(\bar{l},\bar{r}\right)=\frac{(-1)^n}{2}\frac{\bar{r}^2g_i^{(k)}\left(0,\bar{l}\right)}{\mathrm{e}^{(-1)^n\bar{l}}\sinh\left(\bar{l}\right)}+\frac{(-1)^{n+1}}{2}\frac{\bar{r}^2g_i^{(k)}\left(1,\bar{l}\right)}{\sinh\left(\bar{l}\right)}+\frac{(-1)^n}{2}\frac{\overline{p_i}^{(k)}\left(0\right)}{\mathrm{e}^{(-1)^n\bar{l}}\sinh\left(\bar{l}\right)}+\frac{(-1)^{n+1}}{2}\frac{\overline{p_i}^{(k)}\left(1\right)}{\sinh\left(\bar{l}\right)}. \tag{22}$$

The first two terms in equation (22) scale as $\bar{r}^2$ and thus are predominant over the last two terms for a narrow annulus. Injecting equation (18) in equation (22) yields $a_{in}^{(k)}\left(\bar{l},\bar{r}\right)\sim\bar{r}^2a_n\left(l,w_i^{(k)}\right)$ with

$$a_n\left(l,w_i^{(k)}\right)=\frac{1}{1+(-1)^k(\lambda_i/l)^2}\frac{(-1)^n\mathrm{e}^{(-1)^{n+1}\frac{l}{2}}}{2\sinh\left(l\right)}\left[w_i^{(k)}\left(0\right)\mathrm{e}^{(-1)^{n+1}\frac{l}{2}}-w_i^{(k)}\left(1\right)\mathrm{e}^{-(-1)^{n+1}\frac{l}{2}}\right]. \tag{23}$$

Finally, from $\langle p_i\rangle=(-1)^{i+1}\,\overline{p_i}/N_i\cos\left(\theta\right)$, and assuming that $p_i=\langle p_i\rangle$, the dimensionless pressure in the narrow channel writes

$$p_i\left(x,\theta\right)\underset{\varepsilon\to1}{\sim}-(-1)^{i+1}\frac{1}{(\varepsilon-1)^2}\frac{1}{N_i}\sum_{k=1}^{2}\left[g_i^{(k)}\left(x,l\right)+\sum_{n=1}^{2}a_n\left(l,w_i^{(k)}\right)\mathrm{e}^{(-1)^nlx}\right]\cos\left(\theta\right). \tag{24}$$

4. Fluid force matrix

In the previous section, we have obtained an analytical expression of the pressure field in the narrow duct. We now proceed with the determination of the fluid forces acting on the two cylinders. Inserting equation (24) in equation (6) shows that the dimensionless fluid force $\mathbf{f}_{ij}$ has no component along the $\mathbf{e}_x$ direction, i.e. $\mathbf{f}_{ij}\cdot\mathbf{e}_x$=0, whereas the $\mathbf{e}_y$ component writes

$$\left(\mathbf{f}_{ij}\cdot\mathbf{e}_y\right)\underset{\varepsilon\to1}{\sim}\frac{1}{\varepsilon-1}\begin{pmatrix}f\left(l,w_1\right) & -f\left(l,w_2\right)\\ -f\left(l,w_1\right) & f\left(l,w_2\right)\end{pmatrix}. \tag{25}$$

The dimensionless force coefficient $f\left(l,w_j\right)$ depends on both the aspect ratio l and the vibration mode w_j and writes

$$\begin{aligned}f\left(l,w_j\right)&=\frac{1}{N_j}\sum_{k=1}^{2}\frac{1}{1+(-1)^k(\lambda_j/l)^2}\int_0^1w_j^{(k)}\left(x\right)dx+\frac{1}{N_j}\sum_{k=1}^{2}\sum_{n=1}^{2}a_n\left(l,w_j^{(k)}\right)\int_0^1\mathrm{e}^{(-1)^nlx}dx,\\&=\frac{1}{N_j}\frac{1}{\sinh\left(l\right)}\left[\chi_j^{(1)}\left(\frac{\left(1-\cosh\left(l\right)\right)\left(1+\cosh\left(\lambda_j\right)\right)}{l}+\frac{\sinh\left(l\right)\sinh\left(\lambda_j\right)}{\lambda_j}\right)\frac{1}{1-\left(\lambda_j/l\right)^2}\right.\\&\qquad+\chi_j^{(2)}\left(\frac{\left(1-\cosh\left(l\right)\right)\left(1+\cos\left(\lambda_j\right)\right)}{l}+\frac{\sinh\left(l\right)\sin\left(\lambda_j\right)}{\lambda_j}\right)\frac{1}{1+\left(\lambda_j/l\right)^2}\\&\qquad+\chi_j^{(3)}\left(\frac{\left(1-\cosh\left(l\right)\right)\sinh\left(\lambda_j\right)}{l}+\frac{\sinh\left(l\right)\left(\cosh\left(\lambda_j\right)-1\right)}{\lambda_j}\right)\frac{1}{1-\left(\lambda_j/l\right)^2}\\&\qquad\left.+\chi_j^{(4)}\left(\frac{\left(1-\cosh\left(l\right)\right)\sin\left(\lambda_j\right)}{l}+\frac{\sinh\left(l\right)\left(1-\cos\left(\lambda_j\right)\right)}{\lambda_j}\right)\frac{1}{1+\left(\lambda_j/l\right)^2}\right].\end{aligned} \tag{26}$$

The dimensionless fluid force acting on an infinitely long cylinder is obtained by taking the limit of equation (26) as $l \to \infty$. It yields

$$\begin{aligned} f(l, w_j) \underset{l\to\infty}{\to} f(w_j) &= \frac{1}{N_j} \int_0^1 w_j(x) dx, \\ &= \frac{1}{N_j} \left[\chi_j^{(1)} \sinh(\lambda_j) + \chi_j^{(2)} \sin(\lambda_j) + \chi_j^{(3)} (\cosh(\lambda_j) - 1) + \chi_j^{(4)} (1 - \cos(\lambda_j)) \right] \frac{1}{\lambda_j}. \end{aligned} \tag{27}$$

In Figs. 3, 4, and 5, we show the evolution of the dimensionless fluid force coefficient, $f(l, w_j)$, as a function of the aspect ratio l, for various types of boundary conditions listed in Table A.7. We observe that $f(l, w_j)$ exhibits very different behaviors (positive, negative, monotonic, or non-monotonic function of l, slow or fast approach of the asymptotic limit of equation (27) as $l \to \infty$) depending on the boundary conditions and the wave-number of the imposed vibration mode. It is worth to emphasize that the sign of $f(l, w_j)$ determines the direction of the fluid force relative to the imposed displacement. In fact, if $f(l, w_j)$ is positive; see for example the sliding-pinned case, first and third vibration modes; the fluid force acting on the moving cylinder $\mathcal{C}_j$ (resp. the stationary cylinder $\mathcal{C}_i$, $i \neq j$) has the same (resp. opposite) direction as the displacement. On the other hand, if $f(l, w_j)$ is negative; see for example the sliding-pinned case, second vibration mode; the self (resp. cross) fluid force and the imposed displacement have opposite (resp. the same) directions.

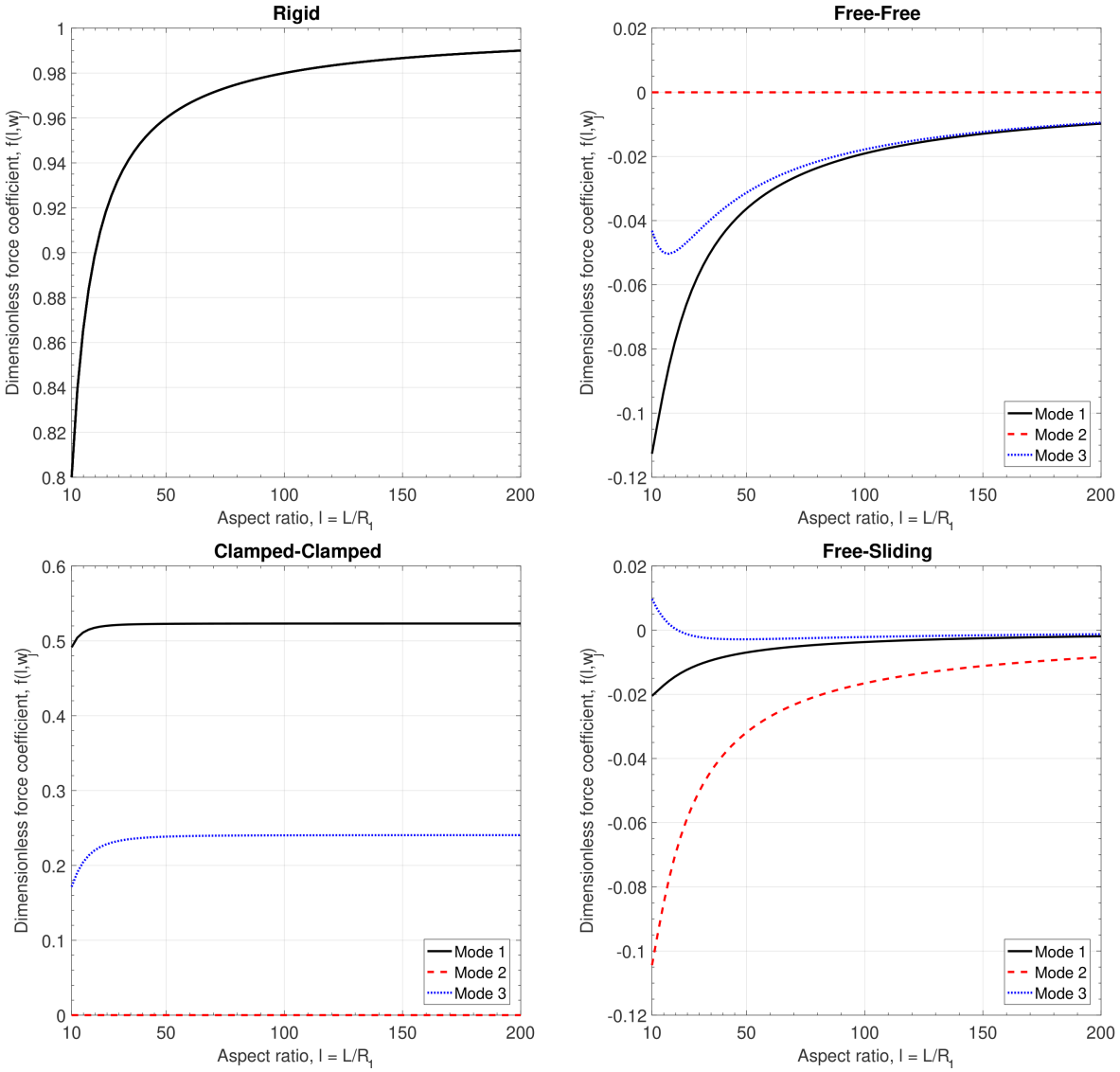

Figure 3: Evolution of the theoretical dimensionless force coefficient, $f(l, w_j)$, given by (26), as a function of the aspect ratio, $l = L/R_1$, for various types of boundary conditions and vibration modes.

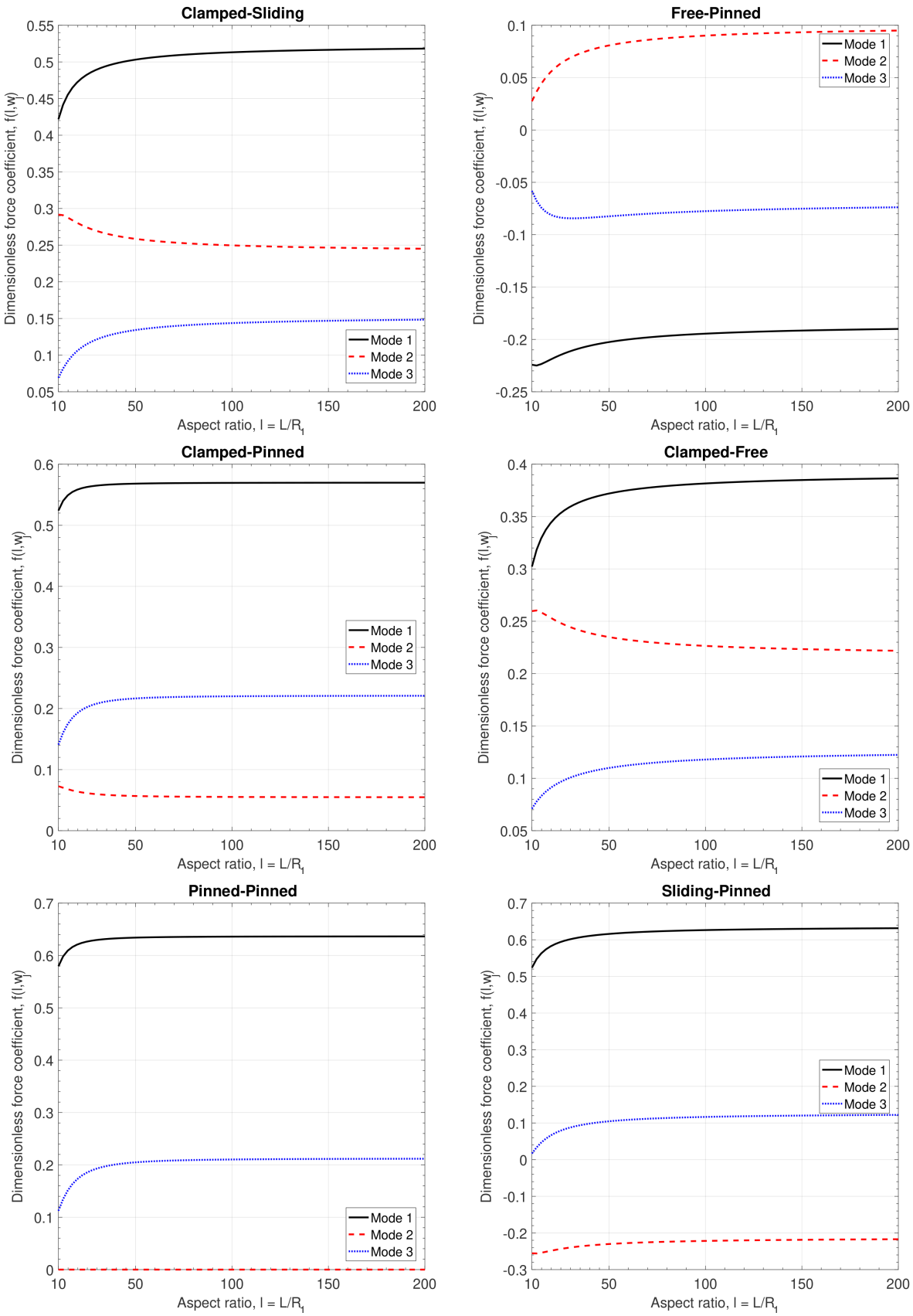

Figure 4: Evolution of the theoretical dimensionless force coefficient, $f(l, w_j)$, given by (26), as a function of the aspect ratio, $l = L/R_1$, for various types of boundary conditions and vibration modes.

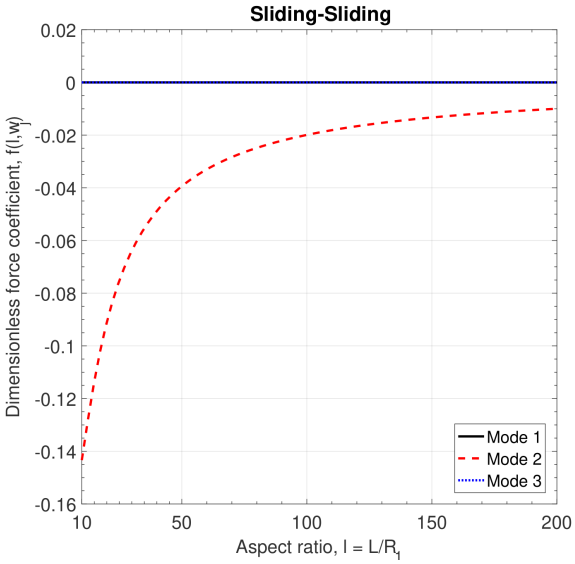

Figure 5: Evolution of the theoretical dimensionless force coefficient, $f(l, w_j)$, given by (26), as a function of the aspect ratio, $l = L/R_1$, for various types of boundary conditions and vibration modes.

5. Comparison to numerical simulations

5.1. TrioCFD

In the previous section, we have provided theoretical predictions for the fluid force matrix, considering different types of boundary conditions. To assess the validity of these predictions, we now perform numerical simulations with the open-source code TrioCFD [17, 18, 19].

The numerical domain is composed of two coaxial oscillating cylinders C_j, with radii R_j and lengths L_j (see Fig. 2). The boundary conditions on the numerical domain consist of imposed displacement on the inner or outer cylinder in the form $\mathbf{Q}(X)\sin(\Omega T)$ and wall boundary conditions on the other.

The numerical simulation does not neglect the convective and viscous terms of the Navier-Stokes equations, contrary to the theoretical approach. The fluid-structure interaction problem involving moving boundaries [20] is solved using an Arbitrary Lagrange-Eulerian method (ALE) [21]. A fluid particle is identified by its position relative to a frame moving with a nonuniform velocity $\mathbf{V}_{ALE}$, and in which the Navier-Stokes equations write

$$\nabla \cdot \mathbf{V} = 0, \tag{28a}$$

$$\frac{\partial J\mathbf{V}}{\partial T} - J\left(\nu\Delta\mathbf{V} - (\mathbf{V}\cdot\nabla)\,\mathbf{V} + (\mathbf{V_{ALE}}\cdot\nabla)\,\mathbf{V} - \frac{1}{\rho}\nabla P\right) = \mathbf{0}, \tag{28b}$$

$$\mathbf{V} - \Omega\mathbf{Q}(X)\cos(\Omega T) = \mathbf{0} \quad \text{on } \partial C_i, \tag{28c}$$

$$\mathbf{V} = \mathbf{0} \quad \text{on } \partial C_j, \quad j \neq i, \tag{28d}$$

where J is the Jacobian of the transformation between the ALE and the Lagrange descriptions. For moderate deformations, $\mathbf{V}_{ALE}$ is usually defined as the solution of an auxiliary Laplace problem

$$\Delta\mathbf{V}_{ALE} = \mathbf{0}, \tag{29a}$$

$$\mathbf{V}_{ALE} - \Omega\mathbf{Q}(X)\cos(\Omega T) = \mathbf{0} \quad \text{on } \partial C_i, \tag{29b}$$

$$\mathbf{V}_{ALE} = \mathbf{0} \quad \text{on } \partial C_j, \quad j \neq i, \tag{29c}$$

from which the kinematics of the mesh grid is updated. The numerical discretization of the system (28) is based on the hybrid Finite Element-Volume method for tetrahedral grids [18, 22]. We denote by $[D]$, $[M]$, $[A]$, $[L(\mathbf{V})]$, and $[G]$ the discrete divergence, mass, diffusion, nonlinear, and gradient matrix operators, respectively. In our simulations, a first-order backward Euler scheme is used to discretize the Navier-Stokes equations, leading to

$$[D]{\mathbf{V}_h}^{n+1} = \mathbf{0}, \tag{30a}$$

$$[M]\frac{\left(J^{n+1}{\mathbf{V}_h}^{n+1} - J^n{\mathbf{V}_h}^n\right)}{\Delta t} - J^{n+1}\left([A]{\mathbf{V}_h}^{n+1} - [L({\mathbf{V}_h}^n)]{\mathbf{V}_h}^{n+1} + [L({\mathbf{V}_h}^n)]{\mathbf{V}_{h,ALE}}^{n+1} - [G]{P_h}^{n+1}\right) = \mathbf{0}, \tag{30b}$$

where $\mathbf{V}_h$ is the discrete fluid velocity, P_h is the discrete fluid pressure, $\mathbf{V}_{h,ALE}$ the discrete mesh velocity, and Δt the time step. The superscripts n and $n+1$ indicate the time step at which the variable is computed.

A second-order upwind MUSCL scheme (Monotonic Upstream-centered Scheme for Conservation Laws, see [23]) is used to approximate the nonlinear convective term $[L(\mathbf{V}_i)]$. A multi-step technique (projection-correction, see [24]) is employed to solve equation (30). The iterative solvers GMRES (Generalized Minimal RESidual method,see [25]), and CGM (Conjugate Gradient Method, see [26]) from the PETSc library (Portable, Extensible Toolkit for Scientific Computation, see [27]) are used for the resolution of the system (30) within the multi-step technique.

The discretization of the domain is based on the mesh generator of the SALOME-platform [28]. We used a locally refined grid of tetrahedrons with two different local sizes were defined: a small local size of 5×10^{-4} m for elements close to the inner cylinder, and a large global size 8×10^{-4} m for other elements. For $l = 15$ and $\varepsilon = 1.1$, the mesh is composed of 1 million tetrahedrons. The time step is 5×10^{-4} s, and the CPU time (Central Processing Unit) is approximately 10 minutes.

5.2. Structure of the fluid force matrix

In this section, we check that the structure of the fluid force matrix, predicted theoretically and given by equation (25) is correct. To do so, we first perform numerical simulations by imposing a vibration mode onto the inner cylinder, and the outer cylinder is fixed. From the numerical fluid force acting on the two cylinders, we extract the coefficients of the first column of the fluid matrix, defined in § 4. Then, we perform numerical simulations by imposing the vibration mode onto the outer cylinder, and the inner cylinder is fixed. From the numerical fluid force acting on the two cylinders, we extract the coefficients of the second column of the fluid force matrix. Comparing the results of these two simulations, we check that the structure of the fluid force matrix obtained numerically is similar to that obtained theoretically, see equation (25). The other numerical parameters are $L_1 = 0.7$ m the length for the inner cylinder, $L_2 = 0.8$ m the length for the outer cylinder, $R_1 = 0.02$ m the radius of the inner cylinder, and $R_2 = 0.022$ m the radius of the outer cylinder. All simulations are performed with an imposed displacement of amplitude $Q = K\,(R_2 - R_1)$, with $K = 2.5$ % and a forcing frequency $\Omega/(2\pi) = 90$ Hz.

The results of this comparative study are presented in Table 1 for the clamped-sliding case and in Table 2 for the free-pinned case. The theoretical approach is entirely linear and inviscid since the convective and viscous terms of the Navier-Stokes equations are neglected. In our numerical simulations, these two terms are nonzero, even if they are kept as small as possible by adjusting the amplitude of the displacement to the size of the annulus and by using a high frequency of oscillation. Nevertheless, the nonlinear term can generate secondary Fourier harmonics that would affect the value of the force matrix. Still, our theory reproduces the force matrix satisfactorily, with a relative deviation that remains acceptable for all configurations tested.

Clamped – **Sliding**	Present theory	Numerics TrioCFD	Relative deviation (%)
$l = 100$	$\begin{pmatrix} 0.5132 & -0.5132 \\ -0.5132 & 0.5132 \end{pmatrix}$	$\begin{pmatrix} 0.5658 & -0.5618 \\ -0.5641 & 0.5700 \end{pmatrix}$	$\begin{pmatrix} 9.30 & 8.65 \\ 9.02 & 9.96 \end{pmatrix}$

Table 1: Structure of the dimensionless fluid force matrix for the first vibration mode of the clamped-sliding case. The aspect ratio is $l = 100$ and the radius ratio is $\varepsilon = 1.1$.

Free – **Pinned**	Present theory	Numerics TrioCFD	Relative deviation (%)
$l = 100$	$\begin{pmatrix} -0.1945 & 0.1945 \\ 0.1945 & -0.1945 \end{pmatrix}$	$\begin{pmatrix} -0.2124 & 0.2097 \\ 0.2107 & -0.2041 \end{pmatrix}$	$\begin{pmatrix} 9.41 & 7.25 \\ 7.69 & 4.70 \end{pmatrix}$

Table 2: Structure of the dimensionless fluid force matrix for the first vibration mode of the free-pinned case. The aspect ratio is $l = 100$ and the radius ratio is $\varepsilon = 1.1$.

Having validated the structure of the fluid force matrix, we now proceed with studying the effect of the radius ratio and the aspect ratio on the $(1,1)$ coefficient. To perform these parametric studies, the inner cylinder is imposed a vibration mode while the outer cylinder is fixed. The $(1,1)$ coefficient is eventually extracted from the numerical fluid force acting on the inner cylinder.

5.3. Effect of the radius ratio

In this section, we assess numerically the validity of the theoretical prediction, equation (26), for the dimensionless fluid force coefficient $f(l, w_j)$, considering three values of the radius ratio, $\varepsilon \in \{1.0375, 1.1, 1.2\}$. Numerical simulations are performed with $R_1 = 0.02$ m and three different external radii, $R_2 \in \{0.02075, 0.022, 0.024\}$ m. The length of the inner cylinder is $L_1 = 0.7$ m, so the aspect ratio is $l = 35$.

The results of this comparative study are presented in Table 3 for the first three vibration modes of the clamped-sliding case and in Table 4 for the free-pinned case. For both cases, we obtain a pretty good agreement between the theoretical prediction and the numerical result; the relative deviation between the two approaches remains less than 17%. For the two cases of boundary conditions, the maximum deviation is always obtained for the least confined configuration, i.e. $\varepsilon = 1.2$. This is mainly due to the fact that our theoretical approach, which is based on the assumption of a narrow annulus, loses precision as ε increases. More specifically, when the annulus becomes wider, the fluid force matrix $(\mathbf{f}_{ij} \cdot \mathbf{e}_y)$ probably exhibits a sensitivity to ε, which is different than $1/(\varepsilon - 1)$, as predicted by the theory, see equation (25).

Clamped – **Sliding**	Present theory	Numerics TrioCFD	Relative deviation (%)
$\varepsilon = 1.0375$	$\begin{pmatrix} 0.4945 \\ 0.2656 \\ 0.1261 \end{pmatrix}$	$\begin{pmatrix} 0.5562 \\ 0.2955 \\ 0.1359 \end{pmatrix}$	$\begin{pmatrix} 11.1 \\ 10.1 \\ 7.21 \end{pmatrix}$
$\varepsilon = 1.1$	$\begin{pmatrix} 0.4945 \\ 0.2656 \\ 0.1261 \end{pmatrix}$	$\begin{pmatrix} 0.5455 \\ 0.2872 \\ 0.1419 \end{pmatrix}$	$\begin{pmatrix} 9.35 \\ 7.52 \\ 11.1 \end{pmatrix}$
$\varepsilon = 1.2$	$\begin{pmatrix} 0.4945 \\ 0.2656 \\ 0.1261 \end{pmatrix}$	$\begin{pmatrix} 0.5653 \\ 0.2953 \\ 0.1481 \end{pmatrix}$	$\begin{pmatrix} 12.52 \\ 10.0 \\ 14.8 \end{pmatrix}$

Table 3: Dimensionless fluid force coefficient, $f(l, w_j)$, for the first three vibration modes of the clamped-sliding case and three values of the radius ratio $\varepsilon = \{1.0375, 1.2, 1.2\}$. The aspect ratio is $l = 35$.

Free – **Pinned**	Present theory	Numerics TrioCFD	Relative deviation (%)
$\varepsilon = 1.0375$	$\begin{pmatrix} -0.2084 \\ 0.07320 \\ -0.08420 \end{pmatrix}$	$\begin{pmatrix} -0.2310 \\ 0.08393 \\ -0.09286 \end{pmatrix}$	$\begin{pmatrix} 9.78 \\ 12.8 \\ 9.32 \end{pmatrix}$
$\varepsilon = 1.1$	$\begin{pmatrix} -0.2084 \\ 0.07320 \\ -0.08420 \end{pmatrix}$	$\begin{pmatrix} -0.2245 \\ 0.08390 \\ -0.08979 \end{pmatrix}$	$\begin{pmatrix} 7.17 \\ 12.8 \\ 6.23 \end{pmatrix}$
$\varepsilon = 1.2$	$\begin{pmatrix} -0.2084 \\ 0.07320 \\ -0.08420 \end{pmatrix}$	$\begin{pmatrix} -0.2307 \\ 0.08823 \\ -0.09175 \end{pmatrix}$	$\begin{pmatrix} 9.67 \\ 17.0 \\ 8.23 \end{pmatrix}$

Table 4: Dimensionless fluid force coefficient, $f(l, w_j)$, for the first three vibration modes of the free-pinned case and three values of the radius ratio $\varepsilon = \{1.0375, 1.1, 1.2\}$. The aspect ratio is $l = 35$.

5.4. Effect of the aspect ratio

In this section, we compare theoretical and numerical predictions for the dimensionless fluid force coefficient $f(l, w_j)$, considering seven values of the aspect ratio, $l \in \{15, 35, 50, 70, 100, 140, 175\}$. The radius ratio is $\varepsilon = 1.1$. Numerical simulations are performed with seven different lengths for the inner cylinder, $L_1 \in \{0.3, 0.7, 1, 1.4, 2, 2.8, 3.5\}$ m, and external cylinder, $L_2 \in \{0.4, 0.8, 1.2, 1.6, 2.2, 3, 3.7\}$ m.

The results of this comparative study are presented in Table 5 for the first three vibration modes of the clamped-sliding case and in Table 6 for the free-pinned case. For the clamped-sliding (resp. free-pinned) case, the maximum relative deviation is 16.1% (resp. 21.9%), and is observed for $l = 15$ and the third (resp. second) mode of vibration. Note that these two maximum relative deviations are computed from very small values of $f(l, w_j)$, and as such, they must be analysed with a very critical eye. In addition to a crude comparison between the theoretical and numerical values of the fluid force coefficient, we show in Fig. 6 that both approaches reproduce the same variations of $f(l, w_j)$ with the aspect ratio l. For the clamped-sliding case, we show that

$f(l, w_j)$ is always positive and is a monotonic increasing (resp. decreasing) function of the aspect ratio for the first and third (resp. second) modes of vibration. For the free-pinned case, the sign and the variations of $f(l, w_j)$ are shown to depend on the wave-number of the vibration mode. In fact, for the first (resp. second) mode, we show that $f(l, w_j)$ is negative (resp. positive) and increases with the aspect ratio l. For the third mode of vibration, $f(l, w_j)$ is negative, and exhibits a non-monotonic evolution, i.e. $f(l, w_j)$ first decreases for small values of l, hits a minimum, and then increases to the asymptotic limit of an infinitely long cylinder. Finally, the good reproduction of the variations and values of $f(l, w_j)$ led us to the conclusion that our analytical expression, equation (26), is a good approximation of the fluid force coefficient, thereby validating our theoretical approach.

Clamped – **Sliding**	Present theory	Numerics TrioCFD	Relative deviation (%)
$l = 15$	$\begin{pmatrix} 0.4560 \\ 0.2874 \\ 0.0923 \end{pmatrix}$	$\begin{pmatrix} 0.5077 \\ 0.3061 \\ 0.1100 \end{pmatrix}$	$\begin{pmatrix} 10.2 \\ 6.11 \\ 16.1 \end{pmatrix}$
$l = 35$	$\begin{pmatrix} 0.4945 \\ 0.2656 \\ 0.1261 \end{pmatrix}$	$\begin{pmatrix} 0.5455 \\ 0.2872 \\ 0.1419 \end{pmatrix}$	$\begin{pmatrix} 9.35 \\ 7.52 \\ 11.1 \end{pmatrix}$
$l = 50$	$\begin{pmatrix} 0.5031 \\ 0.2586 \\ 0.1343 \end{pmatrix}$	$\begin{pmatrix} 0.5612 \\ 0.2843 \\ 0.1517 \end{pmatrix}$	$\begin{pmatrix} 10.4 \\ 9.04 \\ 11.5 \end{pmatrix}$
$l = 70$	$\begin{pmatrix} 0.5089 \\ 0.2536 \\ 0.1397 \end{pmatrix}$	$\begin{pmatrix} 0.5590 \\ 0.2756 \\ 0.1548 \end{pmatrix}$	$\begin{pmatrix} 8.96 \\ 7.98 \\ 9.75 \end{pmatrix}$
$l = 100$	$\begin{pmatrix} 0.5132 \\ 0.2497 \\ 0.1437 \end{pmatrix}$	$\begin{pmatrix} 0.5658 \\ 0.2733 \\ 0.1594 \end{pmatrix}$	$\begin{pmatrix} 9.30 \\ 8.64 \\ 9.85 \end{pmatrix}$
$l = 140$	$\begin{pmatrix} 0.5160 \\ 0.2471 \\ 0.1464 \end{pmatrix}$	$\begin{pmatrix} 0.5687 \\ 0.2708 \\ 0.1620 \end{pmatrix}$	$\begin{pmatrix} 9.27 \\ 8.75 \\ 9.63 \end{pmatrix}$
$l = 175$	$\begin{pmatrix} 0.5174 \\ 0.2458 \\ 0.1477 \end{pmatrix}$	$\begin{pmatrix} 0.5717 \\ 0.2704 \\ 0.1638 \end{pmatrix}$	$\begin{pmatrix} 9.50 \\ 9.10 \\ 9.83 \end{pmatrix}$

Table 5: Dimensionless force coefficient, $f(l, w_j)$, for the first three vibration modes of the clamped-sliding case and seven values of the aspect ratio $l = \{15, 35, 50, 70, 100, 140, 175\}$. The radius ratio is $\varepsilon = 1.1$.

Free – Pinned	Present theory	Numerics TrioCFD	Relative deviation (%)
$l = 15$	$\begin{pmatrix} -0.2234 \\ 0.04460 \\ -0.07440 \end{pmatrix}$	$\begin{pmatrix} -0.2379 \\ 0.05712 \\ -0.08102 \end{pmatrix}$	$\begin{pmatrix} 6.10 \\ 21.9 \\ 8.17 \end{pmatrix}$
$l = 35$	$\begin{pmatrix} -0.2084 \\ 0.07320 \\ -0.08420 \end{pmatrix}$	$\begin{pmatrix} -0.2245 \\ 0.08390 \\ -0.08979 \end{pmatrix}$	$\begin{pmatrix} 7.17 \\ 12.8 \\ 6.23 \end{pmatrix}$
$l = 50$	$\begin{pmatrix} -0.2025 \\ 0.08080 \\ -0.08240 \end{pmatrix}$	$\begin{pmatrix} -0.2220 \\ 0.09232 \\ -0.08938 \end{pmatrix}$	$\begin{pmatrix} 8.78 \\ 12.5 \\ 7.81 \end{pmatrix}$
$l = 70$	$\begin{pmatrix} -0.1981 \\ 0.08610 \\ -0.08000 \end{pmatrix}$	$\begin{pmatrix} -0.2147 \\ 0.09618 \\ -0.08592 \end{pmatrix}$	$\begin{pmatrix} 7.73 \\ 10.5 \\ 6.89 \end{pmatrix}$
$l = 100$	$\begin{pmatrix} -0.1945 \\ 0.09010 \\ -0.07750 \end{pmatrix}$	$\begin{pmatrix} -0.2124 \\ 0.1005 \\ -0.08395 \end{pmatrix}$	$\begin{pmatrix} 9.41 \\ 10.3 \\ 7.68 \end{pmatrix}$
$l = 140$	$\begin{pmatrix} -0.1920 \\ 0.09290 \\ -0.07550 \end{pmatrix}$	$\begin{pmatrix} -0.2100 \\ 0.1031 \\ -0.08208 \end{pmatrix}$	$\begin{pmatrix} 8.57 \\ 9.89 \\ 8.01 \end{pmatrix}$
$l = 175$	$\begin{pmatrix} -0.1907 \\ 0.09430 \\ -0.07440 \end{pmatrix}$	$\begin{pmatrix} -0.2094 \\ 0.1048 \\ -0.08124 \end{pmatrix}$	$\begin{pmatrix} 8.93 \\ 10.0 \\ 8.42 \end{pmatrix}$

Table 6: Dimensionless force coefficient, $f(l, w_j)$, for the first three vibration modes of the free-pinned case and seven values of the aspect ratio $l = \{15, 35, 50, 70, 100, 140, 175\}$. The radius ratio is $\varepsilon = 1.1$.

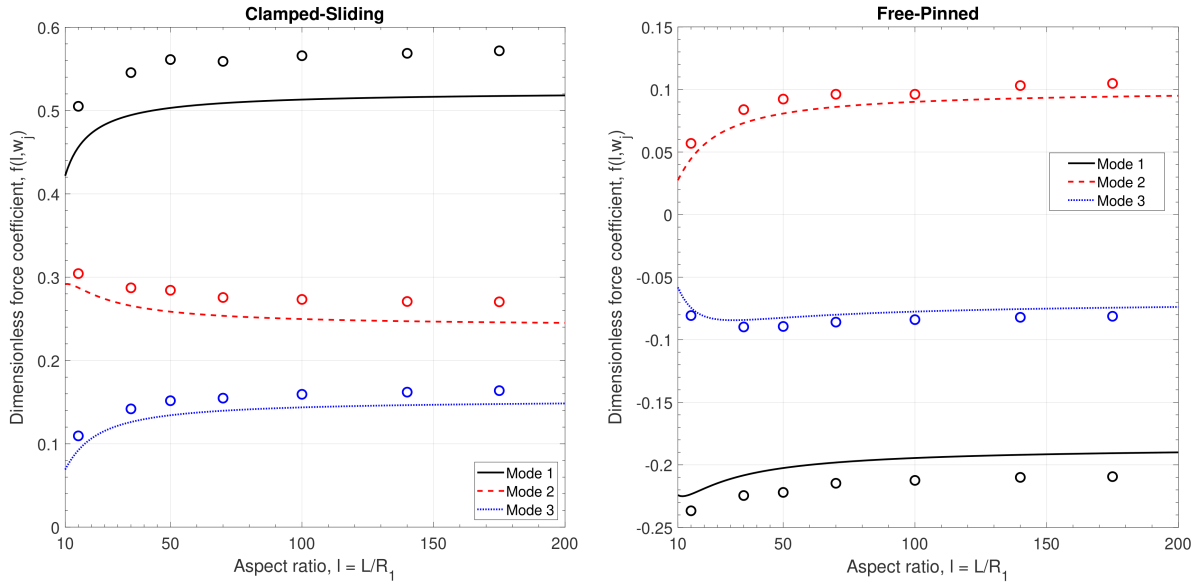

Figure 6: Evolution of the dimensionless force coefficient, $f(l, w_j)$, as a function of the aspect ratio, $l = L/R_1$, for the first three modes of the clamped-sliding and free-pinned boundary conditions. Lines correspond to the theoretical prediction, equation (26), and open circles correspond to the numerical simulations.

6. Conclusion

We have considered the fluid-structure interaction problem of two flexible coaxial cylinders separated by a thin layer of an inviscid fluid. The cylinders have a finite length and are imposed a small harmonic displacement corresponding to a vibration mode of an Euler-Bernoulli beam. Based on the assumption of a narrow annulus,

we have developed a new three-dimensional linear theory to estimate the pressure field in the duct. From the integration of the pressure field, we have obtained a full analytical expression of the fluid force matrix, which is actually shown to be completely determined by a unique coefficient. The sign and variations of this coefficient are shown to strongly depend on the boundary conditions, the wave-number of the vibration modes, and the aspect ratio of the cylinders. All these properties are made explicit in our formulation, covering all types of classical boundary conditions and providing a tractable and straightforward expression of the fluid forces. To assess the validity of our theoretical predictions, we also have performed numerical simulations with the open-source code TrioCFD and its Arbitrary Lagrange-Eulerian implemented method. A thorough and successful comparison was conducted considering different aspect ratios, radius ratios, and two types of boundary conditions.

As a next step, we intend to refine the present theory further to account for the radial variations of the pressure field and, more importantly, to consider the viscous effects in the thin fluid layer. Our approach shall build on our previous work [12] where an Helmholtz decomposition was used to estimate the total fluid force acting on two parallel cylinders.

Acknowledgements

The authors would like to thank P. Piteau for his valuable comments and suggestions to improve the manuscript.

Appendix A. List of the boundary conditions studied

In this appendix, we list in Table A.7 all the types of boundary conditions studied in the present article, providing the parameters associated with the vibration modes.

Boundary Conditions	$\chi^{(k)}$	Wavenumber equation	λ_j	σ	σ_j
Free – Free	$\begin{pmatrix} 1 \\ 1 \\ -\sigma \\ -\sigma \end{pmatrix}$	$\cosh(\lambda)\cos(\lambda) - 1 = 0$	$\begin{pmatrix} 4.7300 \\ 7.8532 \\ 10.996 \end{pmatrix}$	$\frac{\cosh(\lambda)-\cos(\lambda)}{\sinh(\lambda)-\sin(\lambda)}$	$\begin{pmatrix} 0.98250 \\ 1.0008 \\ 0.99997 \end{pmatrix}$
Clamped – Clamped	$\begin{pmatrix} 1 \\ -1 \\ -\sigma \\ \sigma \end{pmatrix}$	$\cosh(\lambda)\cos(\lambda) - 1 = 0$	$\begin{pmatrix} 4.7300 \\ 7.8532 \\ 10.996 \end{pmatrix}$	$\frac{\cosh(\lambda)-\cos(\lambda)}{\sinh(\lambda)-\sin(\lambda)}$	$\begin{pmatrix} 0.98250 \\ 1.0008 \\ 0.99997 \end{pmatrix}$
Free – Sliding	$\begin{pmatrix} 1 \\ 1 \\ -\sigma \\ -\sigma \end{pmatrix}$	$\tanh(\lambda) + \tan(\lambda) = 0$	$\begin{pmatrix} 2.3650 \\ 5.4978 \\ 8.6394 \end{pmatrix}$	$\frac{\sinh(\lambda)-\sin(\lambda)}{\cosh(\lambda)+\cos(\lambda)}$	$\begin{pmatrix} 0.98250 \\ 0.99997 \\ 1.0000 \end{pmatrix}$
Clamped – Sliding	$\begin{pmatrix} 1 \\ -1 \\ -\sigma \\ \sigma \end{pmatrix}$	$\tanh(\lambda) + \tan(\lambda) = 0$	$\begin{pmatrix} 2.3650 \\ 5.4978 \\ 8.6394 \end{pmatrix}$	$\frac{\sinh(\lambda)-\sin(\lambda)}{\cosh(\lambda)+\cos(\lambda)}$	$\begin{pmatrix} 0.98250 \\ 0.99997 \\ 1.0000 \end{pmatrix}$
Free – Pinned	$\begin{pmatrix} 1 \\ 1 \\ -\sigma \\ -\sigma \end{pmatrix}$	$\tan(\lambda) - \tanh(\lambda) = 0$	$\begin{pmatrix} 3.9266 \\ 7.0686 \\ 10.210 \end{pmatrix}$	$\frac{\cosh(\lambda)-\cos(\lambda)}{\sinh(\lambda)-\sin(\lambda)}$	$\begin{pmatrix} 1.0008 \\ 1.0000 \\ 1.0000 \end{pmatrix}$
Clamped – Pinned	$\begin{pmatrix} 1 \\ -1 \\ -\sigma \\ \sigma \end{pmatrix}$	$\tan(\lambda) - \tanh(\lambda) = 0$	$\begin{pmatrix} 3.9266 \\ 7.0686 \\ 10.210 \end{pmatrix}$	$\frac{\cosh(\lambda)-\cos(\lambda)}{\sinh(\lambda)-\sin(\lambda)}$	$\begin{pmatrix} 1.0008 \\ 1.0000 \\ 1.0000 \end{pmatrix}$
Clamped – Free	$\begin{pmatrix} 1 \\ -1 \\ -\sigma \\ \sigma \end{pmatrix}$	$\cosh(\lambda)\cos(\lambda) + 1 = 0$	$\begin{pmatrix} 1.8751 \\ 4.6941 \\ 7.8548 \end{pmatrix}$	$\frac{\cosh(\lambda)+\cos(\lambda)}{\sinh(\lambda)+\sin(\lambda)}$	$\begin{pmatrix} 0.73410 \\ 1.0185 \\ 0.99922 \end{pmatrix}$
Pinned – Pinned	$\begin{pmatrix} 0 \\ 0 \\ 0 \\ 1 \end{pmatrix}$	$\lambda_j = j\pi$	$\begin{pmatrix} \pi \\ 2\pi \\ 3\pi \end{pmatrix}$	X	X
Sliding – Pinned	$\begin{pmatrix} 0 \\ 1 \\ 0 \\ 0 \end{pmatrix}$	$\lambda_j = \frac{(2j-1)\pi}{2}$	$\begin{pmatrix} \pi/2 \\ 3\pi/2 \\ 5\pi/2 \end{pmatrix}$	X	X
Sliding – Sliding	$\begin{pmatrix} 0 \\ 1 \\ 0 \\ 0 \end{pmatrix}$	$\lambda_j = j\pi$	$\begin{pmatrix} \pi \\ 2\pi \\ 3\pi \end{pmatrix}$	X	X

Table A.7: Boundary conditions studied in the present work. The vibration modes are of the form $w_j(x) = \chi^{(1)}\cosh(\lambda_j x) + \chi^{(2)}\cos(\lambda_j x) + \chi_j^{(3)}\sinh(\lambda_j x) + \chi_j^{(4)}\sin(\lambda_j x)$, with $\chi^{(k)}$ given in the first column.

References

[1] Y. Bergamaschi, Y. Bouilloux, P. Chantoin, B. Guigon, X. Bravo, C. Germain, M. Rommens, P. Tremodeux, Jules horowitz reactor, basic design, in: Proc. of ENC, 2002.

[2] R. J. Fritz, The Effect of Liquids on the Dynamic Motions of Immersed Solids, Journal of Engineering for Industry 94 (1) (1972) 167–173.

[3] M. P. Paidoussis, S. J. Price, E. de Langre, Fluid-Structure Interactions: Cross-Flow-Induced Instabilities, Cambridge University Press, 2010.

[4] M. P. Paidoussis, Fluid-structure interactions : slender structures and axial flow. Volume 1, 2nd Edition, Elsevier, London, 2014.

[5] M. P. Paidoussis, Fluid-structure interactions. Volume 2 : slender structures and axial flow, 2nd Edition, Academic Press, London, England, 2016.

[6] R. D. Blevins, Flow-induced vibration, 2nd Edition, Krieger Publishing Company, 1990.

[7] S. S. Chen, Flow-induced vibration of circular cylindrical structures, Hemisphere Pub. Corp, 1987.

[8] F. Axisa, J. Antunes, Modelling of Mechanical Systems: Fluid-structure Interaction, Butterworth-Heinemann Ltd, 2006.

[9] M. P. Paidoussis, Dynamics of cylindrical structures subjected to axial flow, Journal of Sound and Vibration 29 (1973) 365–385.

[10] S. S. Chen, Dynamics of heat exchanger tube banks, Journal of Fluids Engineering. 99 (1977) 462–469.

[11] R. Lagrange, X. Delaune, P. Piteau, L. Borsoi, J. Antunes, A new analytical approach for modeling the added mass and hydrodynamic interaction of two cylinders subjected to large motions in a potential stagnant fluid, Journal of Fluids and Structures. 77 (2018) 102–114.

[12] R. Lagrange, Y. Fraigneau, New estimations of the added mass and damping of two cylinders vibrating in a viscous fluid, from theoretical and numerical approaches, Journal of Fluids and Structures. 92 (2020) 102818.

[13] M. Paidoussis, M.Ostoja-Starzewski, Dynamics of a flexible cylinder in subsonic axial flow, AIAA Journal.

[14] D. Mateescu, M. P. Paidoussis, Annular-flow-induced vibrations of an axially variable body of revolution in a duct of variable crosssection, in: Proceedings of the ASME Symposium on Flow-Induced Vibrations, Vol. 4, 1984, pp. 53–69.

[15] M. P. Paidoussis, D. Mateescu, W.-G. Sim, Dynamics and Stability of a Flexible Cylinder in a Narrow Coaxial Cylindrical Duct Subjected to Annular Flow, Journal of Applied Mechanics 57 (1) (1990) 232–240.

[16] M. Laurens, Présentation IFS. Bloc Pile RJH, 2020, TA–6515496 Ind. A.

[17] P. E. Angeli, U. Bieder, G. Fauchet, Overview of the TrioCFD code: Main features, V&V procedures and typical applications to nuclear engineering, in: Proceedings of 16th International Topical Meeting on Nuclear Reactor Thermal Hydraulics (NURETH-16), Chicago, USA., 2015, p. 252.

[18] P. E. Angeli, M. A. Puscas, G. Fauchet, A. Cartalade, FVCA8 benchmark for the Stokes and Navier-Stokes equations with the TrioCFD code – benchmark session, in: Finite Volumes for Complex Applications VIII - Methods and Theoretical Aspects., 2017, pp. 181–202.

[19] D. Panunzio, M. A. Puscas, R. Lagrange, FSI-Vibrations of immersed cylinders. Simulations with the engineering open-source code TrioCFD. Test cases and experimental comparisons, arXiv 2101.11322.

[20] M. A. Puscas, L. Monasse, A. Ern, C. Tenaud, C. Mariotti, A conservative embedded boundary method for an inviscid compressible flow coupled with a fragmenting structure, International Journal for Numerical Methods in Engineering. 103 (2015) 970–995.

[21] J. Donea, A. Huerta, J. P. Ponthot, A. Rodríguez-Ferran, Arbitrary Lagrangian–Eulerian Methods, American Cancer Society, 2004.

[22] C. Fiorini, B. Després, M. A. Puscas, Sensitivity equation method for the navier-stokes equations applied to uncertainty propagation, International Journal for Numerical Methods in Fluids. (2020) 1–23.

[23] B. Van Leer, Towards the ultimate conservative difference scheme. V. A second-order sequel to Godunov's method, Journal of computational Physics. 32 (1979) 101–136.

[24] A. J. Chorin, Numerical solution of the Navier-Stokes equations, Mathematics of computation. 22 (1968) 745–762.

[25] Y. Saad, M. H. Schultz, GMRES: A generalized minimal residual algorithm for solving nonsymmetric linear systems, SIAM Journal on scientific and statistical computing 7 (3) (1986) 856–869.

[26] M. R. Hestenes, E. Stiefel, Methods of conjugate gradients for solving, Journal of research of the National Bureau of Standards 49 (6) (1952) 409.

[27] S. Balay, S. Abhyankar, M. Adams, J. Brown, P. Brune, K. Buschelman, L. Dalcin, A. Dener, V. Eijkhout, W. Gropp, et al., Petsc users manual, Argonne National Laboratory Technical report.

[28] SALOME-platform, Website: http://www.salome-platform.org/.
URL `http://www.salome-platform.org/`